Observable Two-Step Nucleation Mechanism in Solid-State Formation of Tungsten Carbide

Linfeng Fei,[†] Xianglai Gan,[‡] Sheung Mei Ng,[†] Hui Wang,[†,‡] Ming Xu,[†] Wei Lu,[†] Yanchun Zhou,[§] Chi Wah Leung,[†] Chee-Leung Mak,[*,†] and Yu Wang[*,‡]

† Department of Applied Physics, The Hong Kong Polytechnic University, Hong Kong SAR, China

‡ School of Materials Science and Engineering, Nanchang University, Nanchang, Jiangxi 330031, China

§ Science and Technology on Advanced Functional Composite Laboratory, Aerospace Research Institute of Materials & Processing Technology, Beijing 100076, China

Corresponding Authors

*E-mail: apaclmak@polyu.edu.hk.

*E-mail: wangyu@ncu.edu.cn.

Abstract

The nucleation of crystals from ubiquitous solid-state reactions impacts a wide range of natural and synthetic processes and is fundamental to physical and chemical synthesis. However, the microscopic organization mechanism of amorphous precursors to nanoscale clusters of ordered atoms (nucleus) in an all-solid environment is inaccessible by common experimental probes. Here, by using in situ transmission electron microscopy in combination with theoretical simulations, we show in the reactive formation of a metal carbide that nucleation actually occurs via a two-step mechanism, in which a spinodal-structured amorphous intermediate reorganizes from an amorphous precursor and precedes the emergence of a crystalline nucleus, rather than direct one-step nucleation from classical consideration. We further isolated a series of sophisticated dynamics during formation and development of the nucleus in real-space and interpreted them by thermodynamic favorability. We anticipate that such an indirect organization mechanism which contains a metastable intermedium among the free energy gap between precursors and nanocrystals has its chance in underlying most solid-state crystallizations, whereas the asestablished experimental method represents a step forward in exploring fundamentals in chemical reaction, material engineering, etc.

KEYWORDS:

nanoparticles, crystal nucleation, two-step nucleation, transition metal carbides, tungsten carbide, in situ transmission electron microscopy, in situ heating

The microscopic characteristics of nanomaterials (*e.g.*, size, morphology, and polymorphism), which determine their physicochemical properties to a large extent, are greatly affected by the nucleation and crystal growth processes from precursors. Thorough understanding of the nucleation process is, hence, a crucial step to control the crystallization. Classical consideration of nucleation is based on spontaneous assembly of monomers (atoms, ions, or molecules) toward a nascent nucleus in a single step. (1,2) As the tenets of this classical nucleation theory (CNT) has shown its limitations in a number of complex systems, (3) recent discoveries conceive the notion of nonclassical nucleation, (4−10) which describes multistep pathways containing either prenucleation clusters or amorphous intermediates before the formation of thermodynamically stable nuclei. Particularly, recent technical advancements on transmission electron microscopy (TEM) have made the seminal mechanisms (*i.e.*, Ostwald's step rule, (11) spinodal decomposition, (4,10,12)*etc.*) involved in such nonclassical concepts observable at the nanometer scale, or even atomic scale, across important material systems, for example, calcium carbonate, (10,13,14) calcium phosphate, (8,15) and so on. (16,17) However, reports of such nonclassical pathways are largely based on post-mortem studies or indirect measurements, (9) and the critical dynamics about how the intermediate structure microscopically evolves into a nucleus are still unknown and unconfirmed. Moreover, most previous efforts focused on nucleation scenarios from liquids (driven by either ionic co-precipitation or radiolysis effect from the electron beam); in contrast, direct experimental probing of the nanoscale dynamics concerning early stages of nucleation in alternative states, for instance, solid phase, is rather unexplored due to a lack of validated experimental methods, while it is reasonably essential to constitute a complete picture of nucleation theory.

In response to these fundamental objectives, here, we seek to apply the *in situ* TEM method to follow the step-by-step nucleation dynamics in a solid-state reaction environment; namely, tungsten carbide emerges from carburization of an ultrathin amorphous tungsten/carbon heterostructure. As a result, we discovered a typical two-step nucleation mechanism during the transformation from amorphous W/C heterostructured nanofilms to crystalline tungsten carbide (W_2C) driven by a solid-state reaction. The nucleation was microscopically performed with the formation of spinodal-structured amorphous nanoclusters as an intermediate step, which helps to lower the free energy barrier over the classical one-step pathway. This result confers important implications for understanding nanoscale nucleation and crystallization behaviors and even controlling these events, whereas the technique involved in this study could be potentially applied to relevant processes in materials engineering.

Results

We grew a 10 nm thick amorphous W film *via* magnetron sputtering on a 20 nm thick amorphous carbon film to create a W/C planar heterostructure (see Methods and Figures S1–S3). We then conducted an *in situ* crystallization survey on the W/C heterostructure over a wide temperature range (300–1200 °C; see Figure 1a). Sequential real-time TEM images of Figure 1b–h (the corresponding annealing conditions are denoted in Figure 1a as cyan spheres) exemplify the stepwise morphological evolution of the amorphous W/C heterostructure during a solid-state reaction towards crystalline tungsten carbide nanoparticles. We first noticed the formation of voids (Figure 1c) in the original W film (Figure 1b) at ~690 °C. With the gradual growth of voids, the film subsequently transformed into interpenetrated nanostructures (730 °C, Figure 1d; also refer to Supplementary Movie S1). During this process, the as-formed nanostructures constantly remained amorphous, evidenced by the featureless selected area

electron diffraction (SAED) pattern (inset of Figure 1d). With subsequent ramping, as the voids coalesced and developed into bicontinuous structures (810 °C, Figure 1e), the interpenetrated nanostructures experienced apparent chain breaking and became wormlike structures (1000 °C, Figure 1f). It was also noticeable that the nucleation actually started around this stage, reflected by the weak diffraction rings in the corresponding SAED pattern (inset of Figure 1e, as denoted by the red arrows; diffraction rings expand from 1.4 to 2.3 Å, and the blurred contrast corroborates the nonuniform carbon dispersion in metal) as well as the visible diffraction contrast in the bright-field images (the bright halos around some dark crystals). Upon prolonged annealing at 1000 °C (Figure 1g), the wormlike structures improved their crystallinity to form scattered nanoparticles with a stoichiometric W_2C phase (hexagonal symmetry with space group of $P\bar{3}1m$; see SAED pattern as the inset of Figure 1g, also refer to Figure S4 for the full assignment of this pattern as well as Supplementary Note 1). Further annealing to 1200 °C (Figure 1h) promoted the nanoparticles to reconstruct into faceted ones *via* sophisticated dynamics (refer to Supplementary Movie S2). Additionally, we quantified the coverage of upper layer structures on the C substrate across Figure 1b–h and plotted the result in Figure 1i; the tendency of monotonic decrease suggests the structural conversion from two-dimensional (2D) film to three-dimensional (3D) nanoparticles (*i.e.*, thickness and contact angle increased upon conversion from nanofilm to nanoparticles; also see inset of Figure 1i).

Figure 1. *In situ* annealing sequence. (a) Temperature profile against time for *in situ* annealing experiment. (b–h) Typical bright-field TEM images captured at the respective time in (a) (labeled as cyan spheres) during the solid-state reaction of W/C heterostructure, showing the microscopic structural evolution due to nucleation and crystallization of tungsten carbide. The proposed stage is briefly denoted below the associated image as discussed in the text. The scale

bar in (b) applies to (c–h). The insets in (d), (e), (g), and (h) are their corresponding SAED diffractograms. SAED patterns are shown as negatives to make weak features clear. The red arrows in (f) indicate an arbitrary number of nucleation points within the corresponding spinodal structures. The yellow arrows in (f) indicate examples of nucleation of small spherical droplets. (i) Statistical profile of particle coverage area with respect to the image frames across (b–h). The inset sketches the contact angle (θ) of as-formed nanostructures on the carbon support, which increases throughout (b–h).

The microstructural evolution process presented in Figure 1 is remarkably similar to that observed for microscale spinodal decomposition in isotropic systems. (17−19) Notably, the system, although behaving as liquid-like "viscous flow" in this instance, was indeed at its solid state throughout the experiment as the heating temperature (up to 1200 °C) is far below the melting temperature of 10 nm thick W film (3267 °C; see Figure S5 and the associated discussions). Luthin and Linsmeier have suggested that carbon atoms can dissolve into amorphous tungsten at ∼700 °C; (20) therefore, we consider the spinodal-like structural change to be associated with the solid-state reaction between W and C (*i.e.*, interfacial diffusion). In Figure 1c, carbon and tungsten atoms are thermally activated to commence their diffusional reaction, whereas the net diffusion direction should be the carbon atoms to tungsten film due to the high melting point of W. (21) This unbalanced upward/downward diffusion couple inevitably leads to topological fluctuations to the WC_x overlayer (it is difficult to determine the exact chemical composition here due to the amorphous nature, and the tungsten carbide in this situation is thereby denoted as amorphous WC_x) and hence the formation of voids as well as consequent interpenetrated nanostructures, which is a solid-state spinodal process. Therefore, the driving force here is the compositional gradient within the WC_x overlayer from diffusional

migration of C atoms toward W matrix (*i.e.*, solid-state reaction), which is analogous to density fluctuations that cause spinodal decompositions in liquid solutions. (4,5,10,12) Subsequently, the nucleation of tungsten carbide began to occur, as shown in Figure 1e. Clearly, the nuclei are always located at the WC_x/C interface, implying that heterogeneous nucleation is kinetically preferred over homogeneous nucleation in this case due to lower energy barrier (see text below). (7) As the carbon diffusion continued, all nuclei developed before they grew and the crystallization of WC_x eventually expanded across each nanostructure to form W_2C particles (Figure 1g) and finally induced surface relaxation toward faceted nanoparticles (Figure 1h).

To further resolve the observations, the thermal response of amorphous W/C nanofilms was simulated by molecular dynamics (MD) using the LAMMPS code (22) combined with a reactive force field for the W–C system developed by Juslin *et al.* (23) (see Methods for details). A series of amorphous W/C structures were constructed (Figure S6; also refer to Supplementary Table S2 for the details of the samples) and annealed to understand the process, and one representative result is shown in Figure 2a (plan view) and Figure S7 (side view; also refer to Supplementary Movie S3). Generally, MD simulations show that the amorphous W nanofilm evolves into WC_x nanoparticles *via* amorphous spinodal structures accompanied by continuous invasion of C into W (Figure S8), which is qualitatively consistent with the experimental phenomena. Moreover, such evolving processes are well-reproduced among all nine samples with different thicknesses or densities of W nanofilm, except for the varying speeds of microstructural developments (see Table S2; we show two of them as examples in Figures S9 and S10), clarifying that the indirect pathways are intrinsic in this nucleation. Subsequently, we also evaluated the possibility of crystallization for an amorphous WC_x structure when the W/C atomic ratio reached 2 (x = 1/2). In point of fact, the incurred partial radial distribution functions show

prominent characteristics of ordered W_2C phase with a $P\bar{3}1m$ space group (shown in Figure 2b), in line with the foregoing TEM observations.

Therefore, tungsten carbide nanoparticles nucleate in the solid-state reaction *via* an interesting two-step pathway: amorphous precursor → spinodal-structured amorphous intermediates (SSAIs) → crystalline nucleus, which cannot be reconciled with the notion of CNT (nucleus appears upon encounter of monomers). (1,2) It is noticed that similar two-step mechanisms—for example, liquid → dense liquid droplet → crystalline nucleus, (4,24) or liquid → low-density crystalline nucleus → crystalline nucleus (25)—have been previously claimed from studies of liquid (10,15,26) and colloidal modeling systems. (5,27) However, it is the first observation of such an indirect nucleation process in a solid-state environment, which is of fundamental significance because this implies that the two-step process may be a major mechanism underlying most atomic and molecular systems in 2D and 3D geometries across all three phases.

To grasp more details about the two-step mechanism, we conducted high-resolution TEM (HRTEM) observations to examine the step-by-step mechanisms. We first checked the manner by which the amorphous intermediates are created from the nanofilm. Figure S11 sequentially shows magnified TEM micrographs on the decomposition process of W film to SSAIs during carburization. The gradual enlargement of voids compelled the W film into WC_x SSAIs as an outcome of a range of intense dynamics, which includes splitting, shrinking, rotation, aggregation, and ripening (see also Supplementary Movie S1). The process, despite its occurrence in a solid environment, is basically analogous to recent observations in solutions. (4) It should be mentioned that, subsequently, during the nucleation (started at ~800 °C), a size distribution was developed due to the chain break dynamics caused by Rayleigh instability (28) (also see Figure 1f; the red arrows denote nucleation within large spinodal

structures, and the yellow arrows denote nucleation in small droplets). Upon this circumstance, we then followed the atomic-scale dynamic process of the development of SSAIs into crystalline W_2C nuclei by investigating two aforementioned cases, that is, the nucleation of a large spinodal structure and the nucleation in a small droplet.

First, we followed the nucleation and development mechanisms within a ~7 nm irregular SSAI. As shown in Figure 3a, the WC_x SSAI (area delimited by the cyan line) shows a uniform contrast, suggesting that it is amorphous, which is also supported by the fast Fourier transform (FFT) pattern shown in the inset of Figure 3a. Continuous observation indicates that the SSAI was actually in a metastable state as its outline changed from time to time. We then observed the occurrence of a crystallized cluster (~2 nm, enclosed by the red line) within the SSAI in Figure 3b. The lattice spacing in this embryo is measured as 2.3 Å (inset of Figure 3b), which is consistent with W_2C $(\bar{1}\bar{1}1)$ planes, suggesting that the atomic configuration in this nucleus is identical to that of the bulk crystal (inset of Figure 3f). Notably, the nucleus located at a concave angle within the SSAI (more examples of nucleation at concave regions can be found in Figure S11, indicated by the red arrows). One possible reason is that the geometric characteristics of the concave regions can help to energetically stabilize the nucleus by lowering the free energy barrier during nucleation. (29) Another feature in this process is that the nucleus arose at the SSAI/support interface, showing the nature of heterogeneous nucleation of this event. (30) Thereafter, the nucleus entered the growth phase and grew by consuming the amorphous WC_x matrix until the complete crystallization of the SSAI (Figure 3c–e) to achieve its gradually decreased bulk free energy (ΔG_V; see discussions below), and the advances of the amorphous–crystalline interface keep matching the previous Bravais lattice geometry across the entire structure (compare the FFT patterns in Figure 3b,e). Interestingly, repeated observations

confirmed that crystallization of the SSAIs always finished with a single nucleation event, possibly because the energy barrier required for emergence and successive coalescence of another nucleus inside one SSAI was higher than propagation of a phase front across a distance of several nanometers. (9) This process of formation and development of the nucleus within the metastable amorphous intermediate structure in nonclassical nucleation has been previously predicted in model studies of the 2D crystallization of colloidal microparticles, (24,27) but we report here that such an event is directly observed in real-space at atomic resolution by an *in situ* study (we also recorded a nucleation event within another SSAI with similar characteristics; refer to Figure S12 and the corresponding discussions).

We also tried to trace a complete assembly event from a ∼2 nm nucleus by observing the dynamics of a small amorphous droplet (Figure 4). The reason that motivated us to do this experiment is, we consider that the nucleation of such an isolated particle is absent of disturbance from surrounding WC_x precursors, and the small size of the particle can preserve it at the nucleation stage for a certain period (*i.e.*, practically suppressing size growth) to facilitate our observations. (5) As shown in Figure 4a, initially, an amorphous spherical particle was isolated from other visible precursors. The nucleation of the particle happened after 16 s (Figure 4b), whereby the entire particle rearranged into a poorly ordered structure with substantial defects. Again, the lattice parameters in this small structure were almost identical to that of bulk crystal within our resolution. Subsequent careful examination found frequent events of random surface amorphization (see Figure 4c,d, denoted by red arrows); that is, partial surface of the nucleus became amorphous (or highly disordering) from the crystalline state, and the amorphous part suddenly fluctuated from one side of the particle to another. The disordering fluctuations across the surface can be a result of intrinsic metastability of the nucleus originating from its

comparable size to the critical nucleus size (r_c) in this system. (31−33) However, after prolonged heating (Figure 4e), the nucleus finally evolved into a well-defined, well-ordered truncated cuboctahedron (inset of Figure 4e) by surface relaxation (*e.g.*, surface diffusion) to attain its thermodynamic stability. (34) It is deduced that the stabilization of the nucleus might be achieved with the help of increasing size ($>r_c$) due to possible mass transportation from the surrounding environment, as the size of the final faceted particle is larger than that of the initial nucleus (Figure 4b). We further qualified the nucleation process by calculating the relative crystalline orders of the nucleus from their FFT patterns (refer to Figure S13) with respect to annealing time. (33,35) As plotted in Figure 4f, the nucleus displayed little improvement of crystallinity during the period of surface amorphous fluctuation, whereas it achieved a significant improvement upon faceting, which is in line with the above analysis.

Discussion

A complementary consideration of Figures 3 and 4 establishes a vivid scenario toward a two-step mechanism *via* SSAIs in the nucleation of tungsten carbide. A classical view of the free energy barrier (ΔG) during heterogeneous nucleation is (7)

$$\Delta G = \phi[A\gamma + V\Delta G_V + E_{strain}] \quad (1)$$

where ϕ is a factor dependent on the contact angle between the nucleus and the substrate (inset of Figure 1i), A is the interfacial area, γ is the surface tension, V is the volume of the nucleus, ΔG_V is the Gibbs volume free energy difference between the precursor and the nucleus, and E_{strain} is the misfit strain energy associated with the transformation (it is zero when the parent phase/substrate is a fluid and finite when the parent phase/substrate is a solid). Schematically, the classical nucleation is plotted as the green curve in Figure 3f, and this free energy barrier can be

regarded as barrier 1 (the nucleus with such free energy has the critical nucleus size, r_c). However, in our case, amorphous nuclei (SSAIs) are formed in the first step, followed with an amorphous → crystalline transition of SSAIs to ordered nuclei by atomic rearrangement. The existence of metastable SSAIs buffers the entropy difference between the solid precursor and the crystalline nuclei (E_{strain} decreases, while other terms are considered unchanged in eq 1), and hence the nucleation can be accomplished by overcoming two separated energy barriers (denoted as 2 and 3 in Figure 3f) with significantly decreased ΔG along this indirect pathway (the red line in Figure 3f).

In addition, high-energy electron beams are frequently argued to exert complex effects towards specific samples upon intense illumination. (36−38) Accordingly, in addition to rational experimental operations to avoid high-dose exposure of our interested areas to electron beam (see Methods), we assessed the impact of the electron beam by comparing different areas across the sample during the annealing experiment. It is found, however, a negligible electron beam effect on the whole process throughout nucleation stages of tungsten carbide. We ran the whole heating sequence as in Figure 1a and compared two distant areas (irradiated and unirradiated). The area that received constant illumination possessed a synchronized change of the sample as the area far from electron beam, and they are indeed similar in terms of particle morphology, crystallinity, and size distribution after annealing at 1200 °C for 20 min, as summarized in Figure S14. In other words, the as-observed phenomenom in this work is physically intrinsic and simply driven by thermal stimulation.

Cumulatively, the overall mechanism concerning the early stages of formation of tungsten carbide driven by the solid-state reaction in the W/C heterostructure against temperature and time has been extracted (Figure S15). First, the compact W/C heterostructure commences their

interfacial reaction upon heating. Then, the unbalanced 2D diffusion brings fluctuations to the WC_x overlayer, which decomposes into amorphous spinodal structures (SSAIs). Subsequently, the further accumulation of carbon atoms in WC_x SSAIs toward a stoichiometric ratio leads to the emergence of W_2C nuclei in the SSAI, which is a representative two-step mechanism. Finally, the W_2C nuclei develop themselves by either consuming the SSAIs or absorbing each other (*i.e.*, coalescences; see Figure S16) to individual nanoparticles. Fundamentally, a series of significant physicochemical processes have been disclosed in real-space and at high resolution during the solid-state formation of tungsten carbide, including heterogeneous nucleation, nucleation at concave angles, expansion of atomic ordering across an amorphous structure, surface amorphization, and fluctuation of the nucleus, *etc.*, which we believe should be of pivotal importance in refining modern nucleation theories.

We want to emphasize that the implementation of the current work and the associated deliverables were based on the solid-state observations. Regardless that liquid and solid nucleation processes are of parallel importance for practical applications, compared with prior liquid-cell experiments, (4,10,12,17,39) solid-state observations hold their advantages. First, the diffusion coefficient in a solid can be up to tens of orders of magnitude smaller than that in liquid. It is thus possible that short-lived stages such as vital intermediates (*i.e.*, Figure 3a,b) can be readily identified by simple thermodynamic control. Due to the limited efficiency of mass transport, the microscopic nucleation event can be well-separated from the growth regime by avoiding aggregation of nuclei (*i.e.*, Figure 4). For another example, it was previously uncertain in two-step processes whether monomers in the intermediate clusters reorganize into the nucleus or actually the intermediate clusters act as templates for heterogeneous nucleation of environmental species; (7,40) however, the aforementioned nucleation dynamics (*i.e.*, Figure 3)

indisputably uncover the validity of the former in our solid-state observation due to the absence of external clusters and sluggish dynamics. Second, liquid-cell observations always suffer from random movements (*e.g.*, rotation, drifting) of interested objects in fluidic surroundings, (41) whereas the solid state provides quasi-static background and hence constant sample orientation for crystallographic analysis (*i.e.*, Figure 4). Third, in contrast to limited material systems applicable for liquid-cell experiments (as discussed above), solid-state observations suggest substantial possibilities in a wide range of scenarios beside carbides, especially for the emerging systems such as oxides, 2D materials, and so on. (42) Therefore, we hope the as-established experimental protocol will provide more chances in visualization of atomic-scale nucleation and crystallization mechanisms on the basis of previous studies in liquid environments. It should be further noted that our experimental geometry makes the overall crystallization of tungsten carbide share abundant similarities with modern solid-state methods of material synthesis (especially for thin-film technology), including sputtering deposition, chemical vapor deposition, atomic layer deposition, rapid quenching, *etc.*, and therefore, the method developed here should be of potential suitability in exploring physicochemical processes in these systems.

Conclusions

We have observed the early stages during reactive formation of tungsten carbide from amorphous precursors at elevated temperature, which very clearly shows that a two-step nucleation mechanism involves a spinodal-structured amorphous intermediate. The amorphous intermediate in terms of nanoclusters is a direct precursor to crystalline nuclei in a solid environment and acts as a metastable buffer among the free energy gap between precursors and nanocrystals. Such an indirect pathway for nucleation has its chance in underlying common 2D

and 3D solid-state crystallization, whereas the as-established experimental method offers great potential in exploring fundamentals in chemical reactions, material engineering, *etc*. Our conceptive findings represent a step forward in developing updated nucleation models.

Methods

Specimen Fabrication

Carbon film was predeposited on the heating E-chip. We then prepared W film with a DC magnetron sputtering system (with a base pressure of 1×10^{-3} Pa or better) to construct the W/C heterostructure. W was deposited on the heating E-chip at 20 W with a 0.2 Pa Ar pressure at room temperature.

In Situ TEM Observation

The *in situ* annealing experiment was conducted on a Protochips Fusion platform. TEM observations were made on a JEOL JEM-2100F field-emission transmission electron microscope operating at 200 kV equipped with an Oxford INCA x-sight EDS Si(Li) detector. Prior to every experiment, the specimen was heated to 300 °C and held at this temperature for 60 min to remove any possible adsorbates. For TEM/HRTEM analysis, the sample was heated from 300 °C to a certain temperature. The heating and cooling rate was set as 1.3 and 5 °C s^{-1}, respectively. During the observations, the sample was irradiated by an electron beam with a current density of *ca*. 65 pA cm^{-2}, and the image was recorded by a Gatan Orius SC1000 CCD (charge-coupled device) camera with a short exposure time (~1 s). The electron beam was blanked whenever possible to minimize beam effects on the sample. The *in situ* experiments were implemented twice to confirm the structural dynamics.

MD Simulations

The initial configurations of amorphous W and amorphous C were prepared by moving atoms in body-centered cubic W samples and those in simple cubic C samples with random vectors of lengths less than 2.6 and 1.9 Å, respectively. Then the amorphous W and C were optimized using the conjugate gradient method with the energy and force stopping criteria of 0.5×10^{-3} and 1 eV $Å^{-1}$, respectively. The model parameters of the W and C structures are listed in Table S2. Two typical optimized structures and the corresponding radial distribution functions are presented in Figure S6. Subsequently, the amorphous W/C heterostructures were assembled by conjoining the amorphous C and different thickness amorphous W slices (cut from the amorphous W along the *z* axis). A 1.9 Å gap, which is equal to the equilibrium bond distance of the W–C dimer obtained with the adopted potential, was inserted between the two amorphous blocks, and a 25 Å thick vacuum layer was added on both sides of the *z* boundary. In the MD simulation, the NVT ensemble (constant volume and constant temperature) was imposed on the sample, and the temperature was controlled at 2500 K with the Nosé-Hoover thermostat. (43,44) Periodic boundary condition was set for all directions, and a 1.0 fs time step was adopted for all simulations. To model a semi-infinite amorphous C matrix, the C atoms initially in the bottom 3 Å thick layer were fixed during the simulation. To elucidate the possibility of crystallization for the WC_x mixture, a cubic sample with randomly arranged 4501 W atoms and 2249 C atoms (inset of Figure 2b) was sufficiently melted at 4000 K and subsequently cooled to 800 K within 1.0 ns, and then the structure was analyzed after another 2.0 ns relaxation.

ASSOCIATED CONTENT

Supporting Information

The Supporting Information is available free of charge on the ACS Publications website.

Additional characterizations and experimental data, MD simulation results, supplementary note on reciprocal lattice calculations, captions for supplementary movies (PDF)

Movie S1 (AVI)

Movie S2 (AVI)

Movie S3 (AVI)

AUTHOR INFORMATION

Corresponding Authors *E-mail: apaclmak@polyu.edu.hk. *E-mail: wangyu@ncu.edu.cn.

Author Contributions

L.F., C.-L.M., and Y.W. conceived idea and designed the experiment. X.G. carried out MD simulations. S.M.N. and H.W. prepared TEM samples and conducted AFM analysis. M.X. created schematic figures. L.F. and W.L. conducted TEM experiments. Y.Z. and C.W.L. contributed to discussions. L.F. and Y.W. led experimental data conversion and wrote the manuscript, and all authors commented on it. Y.W. and C.- L.M. supervised implementation of project.

Notes

The authors declare no competing financial interest.

ACKNOWLEDGMENTS

This work was supported by The Hong Kong Polytechnic University (Project Nos. GUA5G, 1-ZVGH, G-YBJ1, and GYPBU) and Nanchang University (Jiangxi Key Laboratory for Two-Dimensional Materials and Devices and Jiangxi Engineering Laboratory for Advanced Functional Thin Films). Financial support from the National Science Foundation of China (Project Nos. 51562026 and 11574126) and Jiangxi's Natural Science Foundation Key Project (Project No. 20171ACB20006) is also acknowledged. We acknowledge use of the facilities within the University Research Facility in Materials Characterization and Device Fabrication (UMF), Centre for Electron Microscopy at The Hong Kong Polytechnic University.

DEDICATION

This paper is dedicated to our dear colleague and friend, Prof. Yu Wang.

Graphical abstract

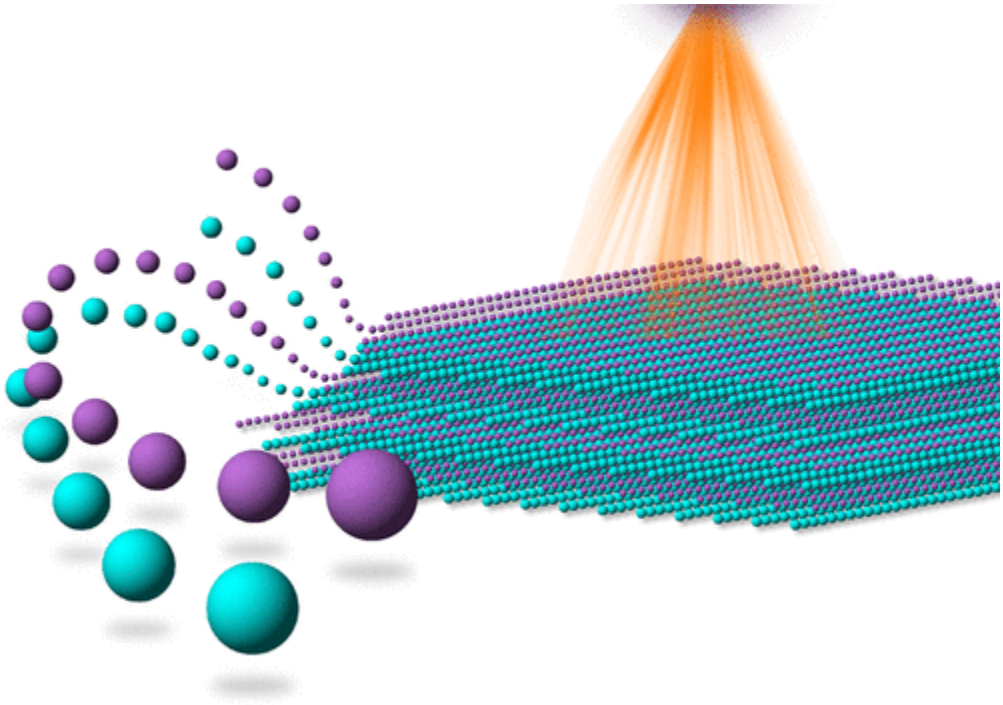

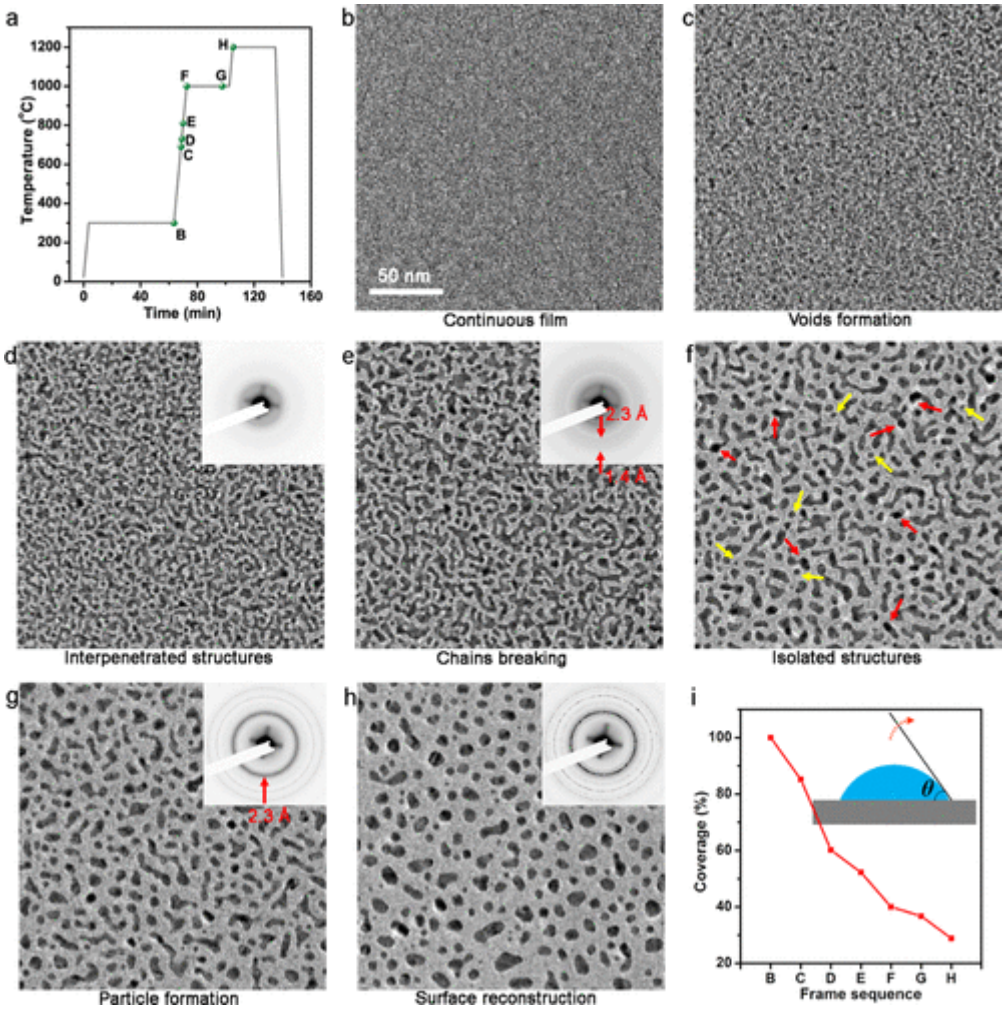

Figure 1. *In situ* annealing sequence. (a) Temperature profile against time for *in situ* annealing experiment. (b–h) Typical bright-field TEM images captured at the respective time in (a) (labeled as cyan spheres) during the solid-state reaction of W/C heterostructure, showing the microscopic structural evolution due to nucleation and crystallization of tungsten carbide. The proposed stage is briefly denoted below the associated image as discussed in the text. The scale bar in (b) applies to (c–h). The insets in (d), (e), (g), and (h) are their corresponding SAED diffractograms. SAED patterns are shown as negatives to make weak features clear. The red arrows in (f) indicate an arbitrary number of nucleation points within the corresponding spinodal structures. The yellow arrows in (f) indicate examples of nucleation of small spherical droplets. (i) Statistical profile of particle coverage area with respect to the image frames across (b–h). The inset sketches the contact angle (θ) of as-formed nanostructures on the carbon support, which increases throughout (b–h).

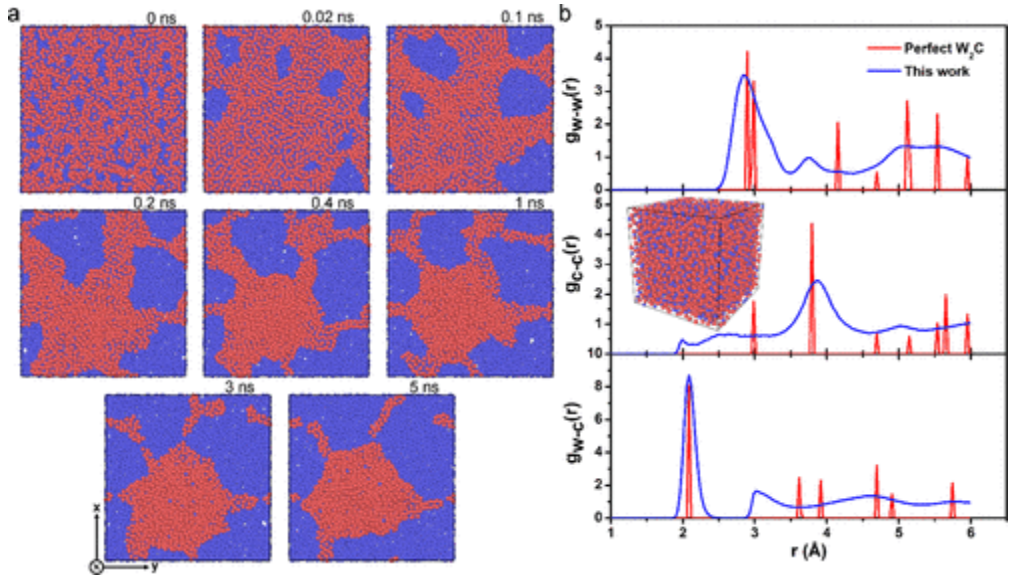

Figure 2. MD simulations of the proposed two-step nucleation. (a) Plan view dynamics of microstructural evolution for the amorphous W/C heterostructure (composed of a 7.4 Å thick amorphous W film and a 19.0 Å thick amorphous C film) *versus* annealing time. The red and blue spheres represent W and C atoms, respectively. See also Figures S7 and S8 for the corresponding side views and Supplementary Movie S3. (b) Comparison of the partial radial distribution functions between perfect W_2C and WC_x mixture (x = 1/2). The inset shows a typical microstructure of the WC_x mixture with a stoichiometric ratio of W_2C used in the MD simulation.

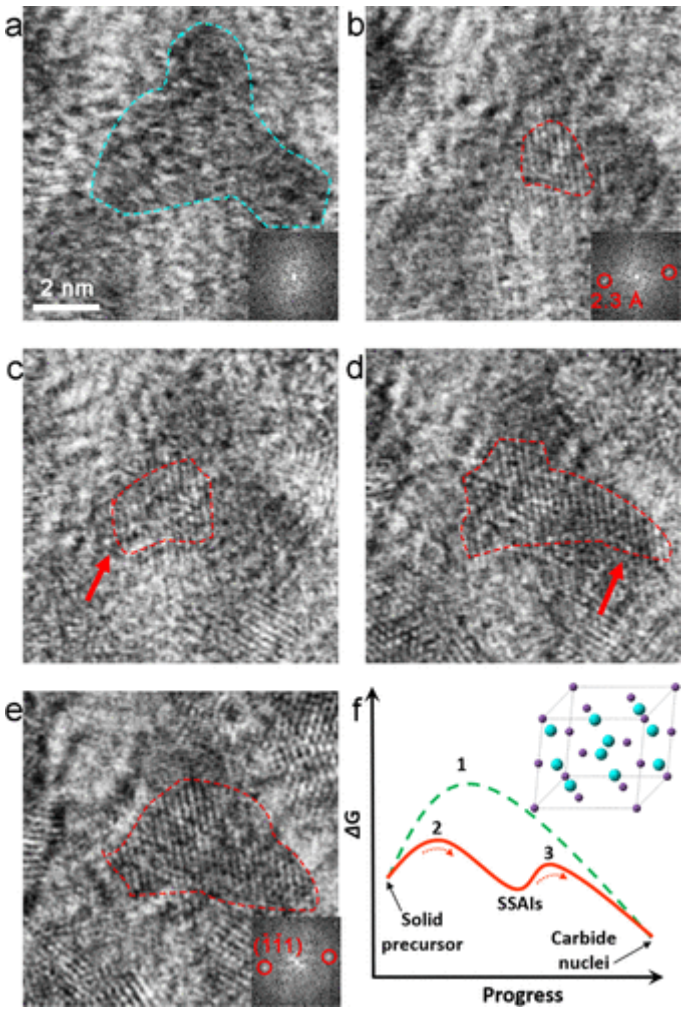

Figure 3. Nucleation mechanism of a SSAI structure. Sequential snapshots of lattice-resolved TEM images showing the representative steps during a nucleation event for a SSAI structure (area delimited by the dashed cyan lines in (a)) during annealing at 700 °C for (a) 0 s, (b) 48 s, (c) 94 s, (d) 165 s, and (e) 272 s. Time listed for all panels is relative to frame (a). The scale bar in (a) applies to (b–e). The areas marked by the dashed red lines in (b–e) correspond to the crystallized domains. The red arrows in (c) and (d) indicate the emerged crystallization area in each step. The insets of (a), (b), and (e) show the corresponding FFT patterns of the structure. The diffraction spots for W_2C phase are denoted by red circles. (f) Free energy (ΔG) profiles during the classical nucleation (green curve) and the two-step nucleation *via* SSAIs (red curve); 1, 2, and 3 denote critical enthalpy barriers. Inset shows the atomic structure for W_2C (JCPDS card no. 65-3896); purple and cyan spheres represent carbon and tungsten atoms, respectively.

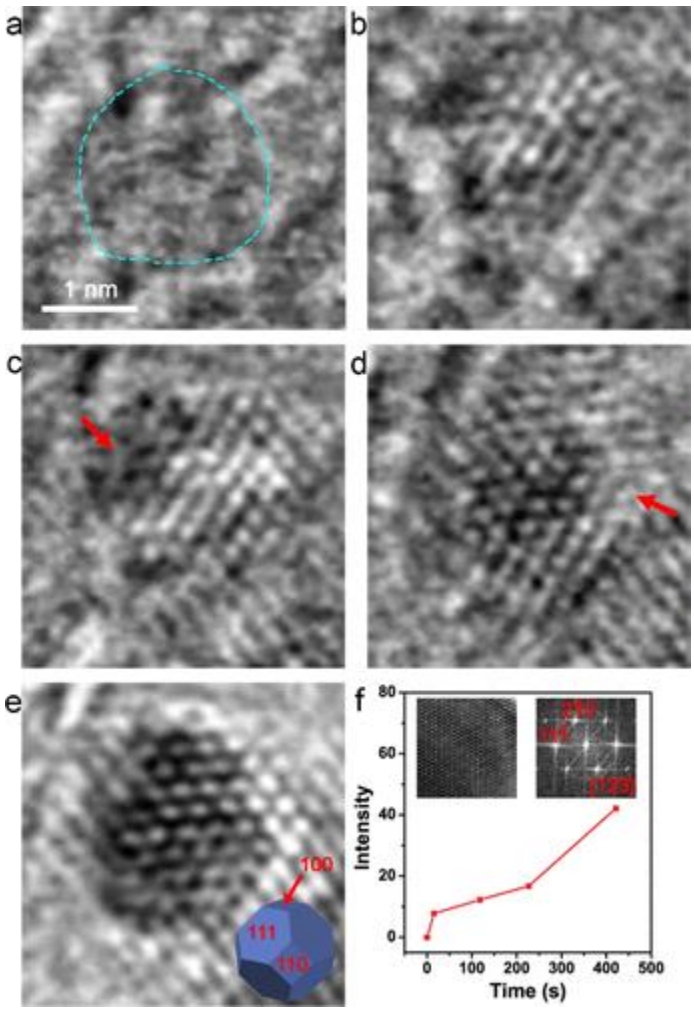

Figure 4. Nucleation and relaxation of a small particle. The bright-field HRTEM images at (a) 0 s, (b) 16 s, (c) 118 s, (d) 227 s, and (e) 421 s upon annealing at 700 °C. Time listed for all panels is relative to frame (a). The area delimited by the dashed cyan line in (a) corresponds to the outline of the amorphous droplet. The scale bar in (a) applies to (b–e). The red arrows in (c) and (d) indicate the fluctuation of surface disordering. The inset in (e) shows a corresponding 3D structural model for W_2C particle as truncated cuboctahedron, enclosed by {100}, {110}, and {111} facets. (f) Evolution of relative crystalline order for nucleus throughout (a–e) against time. The amounts of crystalline order were determined from the integrated profiles of the corresponding FFT patterns (see Figure S8), comparing the value from a nanoparticle with the same crystal orientation (whose crystalline order is set as 100, annealed at 1200 °C for approximate 20 min; the insets of (f) show its lattice image and the corresponding FFT pattern)

REFERENCES

(1) Baumgartner, J.; Dey, A.; Bomans, P. H. H.; Le Coadou, C.; Fratzl, P.; Sommerdijk, N. A. J. M.; Faivre, D. Nucleation and Growth of Magnetite from Solution. Nat. Mater. 2013, 12, 310−314.

(2) Kashchiev, D. Thermodynamically Consistent Description of the Work to Form a Nucleus of Any Size. J. Chem. Phys. 2003, 118, 1837−1851.

(3) Van Driessche, A. E. S.; Benning, L. G.; Rodriguez-Blanco, J. D.; Ossorio, M.; Bots, P.; Garcia-Ruiz, J. M. The Role and Implications of Bassanite as a Stable Precursor Phase to Gypsum Precipitation. Science 2012, 336, 69−72.

(4) Loh, N. D.; Sen, S.; Bosman, M.; Tan, S. F.; Zhong, J.; Nijhuis, C. A.; Kral, P.; Matsudaira, P.; Mirsaidov, U. Multistep Nucleation of Nanocrystals in Aqueous Solution. Nat. Chem. 2016, 9, 77−82.

(5) Lee, J.; Yang, J.; Kwon, S. G.; Hyeon, T. Nonclassical Nucleation and Growth of Inorganic Nanoparticles. Nat. Rev. Mater. 2016, 1, 16034.

(6) De Yoreo, J. J.; Gilbert, P. U. P. A.; Sommerdijk, N. A. J. M.; Penn, R. L.; Whitelam, S.; Joester, D.; Zhang, H.; Rimer, J. D.; Navrotsky, A.; Banfield, J. F.; Wallace, A. F.; Michel, F. M.; Meldrum, F. C.; Colfen, H.; Dove, P. M. Crystallization by Particle Attachment in Synthetic, Biogenic, and Geologic Environments. Science 2015, 349, aaa6760.

(7) Thanh, N. T. K.; Maclean, N.; Mahiddine, S. Mechanisms of Nucleation and Growth of Nanoparticles in Solution. Chem. Rev. 2014, 114, 7610−7630.

(8) Habraken, W. J. E. M.; Tao, J.; Brylka, L. J.; Friedrich, H.; Bertinetti, L.; Schenk, A. S.; Verch, A.; Dmitrovic, V.; Bomans, P. H. H.; Frederik, P. M.; Laven, J.; van der Schoot, P.; Aichmayer, B.; de With, G.; DeYoreo, J. J.; Sommerdijk, N. A. J. M. Ion-Association Complexes Unite Classical and Non-Classical Theories for the Biomimetic Nucleation of Calcium Phosphate. Nat. Commun. 2013, 4, 1507.

(9) Gebauer, D.; Cölfen, H. Prenucleation Clusters and NonClassical Nucleation. Nano Today 2011, 6, 564−584.

(10) Nielsen, M. H.; Aloni, S.; De Yoreo, J. J. In Situ TEM Imaging of CaCO3 Nucleation Reveals Coexistence of Direct and Indirect Pathways. Science 2014, 345, 1158−1162.

(11) Chung, S.-Y.; Kim, Y.-M.; Kim, J.-G.; Kim, Y.-J. Multiphase Transformation and Ostwald's Rule of Stages during Crystallization of a Metal Phosphate. Nat. Phys. 2009, 5, 68−73.

(12) Wallace, A. F.; Hedges, L. O.; Fernandez-Martinez, A.; Raiteri, P.; Gale, J. D.; Waychunas, G. A.; Whitelam, S.; Banfield, J. F.; De Yoreo, J. J. Microscopic Evidence for Liquid-Liquid Separation in Supersaturated CaCO3 Solutions. Science 2013, 341, 885−889.

(13) Gebauer, D.; Volkel, A.; Colfen, H. Stable Prenucleation Calcium Carbonate Clusters. Science 2008, 322, 1819−1822.

(14) Freeman, C. L.; Harding, J. H.; Quigley, D.; Rodger, P. M. Structural Control of Crystal Nuclei by an Eggshell Protein. Angew. Chem., Int. Ed. 2010, 49, 5135−5137.

(15) Nudelman, F.; Pieterse, K.; George, A.; Bomans, P. H. H.; Friedrich, H.; Brylka, L. J.; Hilbers, P. A. J.; de With, G.; Sommerdijk, N. A. J. M. The Role of Collagen in Bone Apatite Formation in the Presence of Hydroxyapatite Nucleation Inhibitors. Nat. Mater. 2010, 9, 1004−1009.

(16) Vekilov, P. G. Phase Diagrams and Kinetics of Phase Transitions in Protein Solutions. J. Phys.: Condens. Matter 2012, 24, 193101.

(17) Schreiber, R. E.; Houben, L.; Wolf, S. G.; Leitus, G.; Lang, Z.- L.; Carbo, J. J.; Poblet, J. M.; Neumann, R. Real-Time Molecular Scale´ Observation of Crystal Formation. Nat. Chem. 2017, 9, 369−373.

(18) Du, B.; Xie, F.; Wang, Y.; Yang, Z.; Tsui, O. K. C. Dewetting of Polymer Films with Built-in Topographical Defects. Langmuir 2002, 18, 8510−8517.

(19) Cahn, J. W. Phase Separation by Spinodal Decomposition in Isotropic Systems. J. Chem. Phys. 1965, 42, 93−99. (20) Luthin, J.; Linsmeier, C. Carbon Films and Carbide Formation on Tungsten. Surf. Sci. 2000, 454−456, 78−82.

(21) Fei, L.; Ng, S. M.; Lu, W.; Xu, M.; Shu, L.; Zhang, W.-B.; Yong, Z.; Sun, T.; Lam, C. H.; Leung, C. W.; Mak, C. L.; Wang, Y. AtomicScale Mechanism on Nucleation and Growth of Mo2C Nanoparticles Revealed by in Situ Transmission Electron Microscopy. Nano Lett. 2016, 16, 7875−7881.

(22) Plimpton, S. Fast Parallel Algorithms for Short-Range Molecular Dynamics. J. Comput. Phys. 1995, 117, 1−19.

(23) Juslin, N.; Erhart, P.; Traskelin, P.; Nord, J.; Henriksson, K. O.¨E.; Nordlund, K.; Salonen, E.; Albe, K. Analytical Interatomic Potential for Modeling Nonequilibrium Processes in the W−C−H System. J. Appl. Phys. 2005, 98, 123520.

(24) Zhang, T. H.; Liu, X. Y. How Does a Transient Amorphous Precursor Template Crystallization. J. Am. Chem. Soc. 2007, 129, 13520−13526.

(25) Tan, P.; Xu, N.; Xu, L. Visualizing Kinetic Pathways of Homogeneous Nucleation in Colloidal Crystallization. Nat. Phys. 2014, 10, 73−79.

(26) Dey, A.; Bomans, P. H. H.; Müller, F. A.; Will, J.; Frederik, P. M.; de With, G.; Sommerdijk, N. A. J. M. The Role of Prenucleation Clusters in Surface-Induced Calcium Phosphate Crystallization. Nat. Mater. 2010, 9, 1010−1014.

(27) Savage, J. R.; Dinsmore, A. D. Experimental Evidence for TwoStep Nucleation in Colloidal Crystallization. Phys. Rev. Lett. 2009, 102, 198302.

(28) Rayleigh, L. On the Instability of Jets. Proc. London Math. Soc. 1878, s1-10, 4−13. (29) Jia, F.; Zhao, D.; Wang, M. Selective Nucleation and SelfOrganized Crystallization. Prog. Cryst. Growth Charact. Mater. 2016, 62, 252−272.

(30) Peng, Y.; Wang, F.; Wang, Z.; Alsayed, A. M.; Zhang, Z.; Yodh, A. G.; Han, Y. Two-Step Nucleation Mechanism in Solid−Solid Phase Transitions. Nat. Mater. 2015, 14, 101−108.

(31) Gilbert, B. Nanoparticles: Strained and Stiff. Science 2004, 305, 651−654.

(32) Chen, X.; Samia, A. C. S.; Lou, Y.; Burda, C. Investigation of the Crystallization Process in 2 nm CdSe Quantum Dots. J. Am. Chem. Soc. 2005, 127, 4372−4375.

(33) Li, Y.; Zang, L.; Jacobs, D. L.; Zhao, J.; Yue, X.; Wang, C. In Situ Study on Atomic Mechanism of Melting and Freezing of Single Bismuth Nanoparticles. Nat. Commun. 2017, 8, 14462.

(34) Marks, L. D.; Peng, L. Nanoparticle Shape, Thermodynamics and Kinetics. J. Phys.: Condens. Matter 2016, 28, 053001.

(35) Horcas, I.; Fernandez, R.; Go´ mez-Rodríguez, J. M.; Colchero,´ J.; Gomez-Herrero, J.; Baro, A. M. WSXM: A Software for Scanning´ Probe Microscopy and a Tool for Nanotechnology. Rev. Sci. Instrum. 2007, 78, 013705.

(36) Tian, X.; Anand, U.; Mirsaidov, U.; Zheng, H. Spontaneous Reshaping and Splitting of AgCl Nanocrystals under Electron Beam Illumination. Small 2018, 1803231.

(37) Zheng, H.; Rivest, J. B.; Miller, T. A.; Sadtler, B.; Lindenberg, A.; Toney, M. F.; Wang, L.-W.; Kisielowski, C.; Alivisatos, A. P. Observation of Transient Structural-Transformation Dynamics in a Cu2S Nanorod. Science 2011, 333, 206−209.

(38) Gonzalez-Martinez, I. G.; Bachmatiuk, A.; Bezugly, V.; Kunstmann, J.; Gemming, T.; Liu, Z.; Cuniberti, G.; Rümmeli, M. H. Electron-Beam Induced Synthesis of Nanostructures: A Review. Nanoscale 2016, 8, 11340−11362.

(39) Liao, H.-G.; Zherebetskyy, D.; Xin, H.; Czarnik, C.; Ercius, P.; Elmlund, H.; Pan, M.; Wang, L.-W.; Zheng, H. Facet Development during Platinum Nanocube Growth. Science 2014, 345, 916−919.

(40) De Yoreo, J. J. A Holistic View of Nucleation and SelfAssembly. MRS Bull. 2017, 42, 525−536.

(41) Fu, X.; Chen, B.; Tang, J.; Hassan, M. T.; Zewail, A. H. Imaging Rotational Dynamics of Nanoparticles in Liquid by 4D Electron Microscopy. Science 2017, 355, 494−498.

(42) Fei, L.; Lei, S.; Zhang, W.; Lu, W.; Lin, Z.; Lam, C. H.; Chai, Y.; Wang, Y. Direct TEM Observations of Growth Mechanisms of Two-Dimensional MoS2 Flakes. Nat. Commun. 2016, 7, 12206.

(43) Nose, S. A Unified Formulation of the Constant Temperature´ Molecular Dynamics Methods. J. Chem. Phys. 1984, 81, 511−519.

(44) Hoover, W. G. Canonical Dynamics: Equilibrium Phase-Space Distributions. Phys. Rev. A: At., Mol., Opt. Phys. 1985, 31, 1695−1697.